

DEEP MIXING AND METALLICITY: CARBON DEPLETION IN GLOBULAR CLUSTER GIANTS

SARAH L. MARTELL AND GRAEME H. SMITH
University of California Observatories/Lick Observatory
Department of Astronomy & Astrophysics, UC Santa Cruz and
1156 High St, Santa Cruz, CA 95064

AND

MICHAEL M. BRILEY
Department of Physics and Astronomy, University of Wisconsin Oshkosh and
800 Algoma Blvd, Oshkosh, WI 54901

Draft version November 4, 2018

ABSTRACT

We present the results of an observational study of the efficiency of deep mixing in globular cluster red giants as a function of stellar metallicity. We determine [C/Fe] abundances based on low-resolution spectra taken with the Kast spectrograph on the 3m Shane telescope at Lick Observatory. Spectra centered on the 4300Å CH absorption band were taken for 42 bright red giants in 11 Galactic globular clusters ranging in metallicity from M92 ([Fe/H]= -2.29) to NGC 6712 ([Fe/H]= -1.01). Carbon abundances were derived by comparing values of the CH bandstrength index $S_2(CH)$ measured from the data with values measured from a large grid of SSG synthetic spectra. Present-day abundances are combined with theoretical calculations of the time since the onset of mixing, which is also a function of stellar metallicity, to calculate the carbon depletion rate across our metallicity range. We find that the carbon depletion rate is twice as high at a metallicity of [Fe/H]= -2.3 than at [Fe/H]= -1.3, which is a result qualitatively predicted by some theoretical explanations of the deep mixing process.

Subject headings: Globular clusters: individual (NGC 4147, NGC 5727, M3, NGC 5904, M5, NGC 6205, M13, NGC 6254, M10, NGC 6341, M92, NGC 6535, NGC 6712, NGC 6779, M56, NGC 7078, M15, NGC 7089, M2) - Stars: abundances - Stars: evolution

1. INTRODUCTION

The observation that carbon abundance in globular cluster red giants declines continuously as the stars evolve has inspired a great deal of observational and theoretical study (e.g., Suntzeff 1981, Carbon et al. 1982, Trefzger et al. 1983, Suntzeff & Smith 1991, Weiss & Charbonnel 2004, Denissenkov & Tout 2000, Smith & Briley 2006, and similar work). Canonically, abundances should be static on the red giant branch after the first dredge-up because of the broad radiative zone between the hydrogen-burning shell and the surface. Progressive carbon depletion with rising luminosity on the giant branch is commonly interpreted as a sign of a non-convective “deep mixing” process that mixes carbon-depleted material from the hydrogen-burning shell, where the CN(O) cycle is acting, to the surface (e.g., Sweigart & Mengel 1979, Charbonnel 1995, Charbonnel et al. 1998, Bellman et al. 2001, Denissenkov & VandenBerg 2003, and others). This same depletion of surface carbon abundance is also observed in red giants in the halo field (e.g., Gratton et al. 2000), and is observed to occur at the same rate in the halo field as in globular clusters with halo-like metallicities (e.g., Smith & Martell 2003).

The process of deep mixing, inferred from observations of low [C/Fe], $\log \epsilon(\text{Li})$, and $^{12}\text{C}/^{13}\text{C}$, is only observed to occur in stars brighter than the red giant branch (RGB) luminosity function “bump” (Charbonnel et al. 1998). There are indications (e.g., Langer et al. 1986, Bellman

et al. 2001) that there may be carbon depletion in stars fainter than the RGB bump in the metal-poor globular cluster M92, though there is not an obvious physical explanation for such a phenomenon. During the first dredge-up, in the subgiant phase, the base of the convective envelope drops inward to smaller radius as the stellar core contracts, mixing the partially-processed material of the stellar interior with the unprocessed material at the surface. As hydrogen shell burning progresses, low on the giant branch, the temperature gradient in the star steepens and the base of the convective envelope begins to move outward, leaving behind a sharp jump in mean molecular weight (the “ μ -barrier”) at the point of its furthest inward progress (Iben 1965). As the convective envelope retreats outward, this steep μ gradient finds itself within a radiative region between the hydrogen-burning shell and the base of the convective zone, where it can potentially hinder mass motions within the radiative zone.

The red giant branch bump is an evolutionary stutter that occurs when the hydrogen-burning shell, which is advancing outward in mass, encounters the μ barrier. The sudden influx of hydrogen-rich material to the hydrogen-burning shell causes the star to become briefly bluer and fainter before it re-equilibrates and continues to evolve along the red giant branch (e.g., Iben 1968, Cassisi et al. 2002). In a collection of stars with equal age and composition, this evolutionary loop will result in an unexpectedly large number of stars at a particular magnitude, and a bump in the differential luminosity function. At a fixed mass, the base of the convective envelope sinks lower in higher-metallicity stars during the first dredge-up, meaning that the RGB bump

occurs at a fainter luminosity on the RGB in high-metallicity globular clusters than in low-metallicity clusters (e.g., Zoccali 1999). However, because evolutionary timescales shorten as stellar mass rises, there is a maximum mass of $\simeq 2M_{\odot}$ for stars to experience this evolutionary loop: above that mass, the hydrogen-burning shell does not move outward far enough to cross the μ barrier in the short time the star is on the RGB (Gilroy 1989). The fact that deep mixing does not begin until after the hydrogen-burning shell crosses the μ barrier is interpreted by, e.g., Charbonnel (1994) to mean that the gradient of mean molecular weight is the dominant factor in permitting or prohibiting deep mixing. Indeed, Denissenkov & Vandenberg (2003) point out that $\nabla\mu$ is “the only physical quantity that changes significantly while approaching the hydrogen-burning shell” in post-bump red giants. Chanamé et al. (2005) provide a somewhat different perspective: in their maximal-mixing models, the μ gradient inhibits mixing on the upper giant branch, but rotational mixing processes are not strong enough on the lower giant branch to cause observable changes in surface abundances, regardless of whether there is a steep μ gradient present.

The underlying physical reason for deep mixing is not clear, though rotation has commonly been implicated since Sweigart & Mengel (1979) proposed meridional circulation as an explanation for CNO anomalies in red giants. Recent theoretical studies tend to focus on specific parametrizations and representations of the process; for example, Rayleigh-Taylor instability (Eggleton et al. 2008), diffusion (Denissenkov & Vandenberg 2003), and thermohaline mixing (Charbonnel & Zahn 2007). Palacios et al. (2006) demonstrated that meridional circulation, differential rotation, and shear turbulence do not create enough mixing to account for the observed variations in surface abundances, implying that additional hydrodynamical processes must be acting. The large study of surface abundances in field giants published by Gratton et al. (2000) is a key to differentiating between models of deep mixing, since it demonstrates clearly the progressive depletion of carbon on the giant branch, as well as the sharp drop in $^{12}\text{C}/^{13}\text{C}$ and $\log \epsilon(\text{Li})$ that happens at the RGB bump.

The fundamental result from Gratton et al. (2000) that all current deep mixing models must reproduce is that deep mixing is universal among post-bump red giants. Charbonnel et al. (1998) consider mixing in terms of the “critical μ gradient,” the largest gradient in mean molecular weight that still permits deep mixing. In an observational study of seven mildly metal-poor red giants in the region of the RGB bump, they find that the critical μ gradient is independent of composition or mass.

Denissenkov & Vandenberg (2003) use the formalism of diffusion, with mixing depth and a diffusion constant as the important parameters, to model deep mixing. They find that the mixing depth does not depend strongly on metallicity, which implies that all red giants with a mass less than $\simeq 2M_{\odot}$ will experience deep mixing. Their figures also show that the evolution of surface abundances of carbon and nitrogen are not particularly affected by metallicity, though reductions in $\log \epsilon(\text{Li})$ and $^{12}\text{C}/^{13}\text{C}$ are more sensitive. Eggleton et al. (2008) show that the reaction ${}^3\text{He}({}^3\text{He}, 2p){}^4\text{He}$ causes a μ -inversion in

the outer edge of the hydrogen-burning shell, and claim that the resulting Rayleigh-Taylor instability is important in driving deep mixing. Charbonnel & Zahn (2007) argue that the more complex process of thermohaline convection will act in that μ -inversion region. They use the Ulrich (1972) prescription to parametrize the thermohaline mixing as a diffusion process. In contrast to Denissenkov & Vandenberg (2003), they find that the evolution of the surface abundances of carbon, nitrogen, and lithium are all affected by overall stellar metallicity, while the $^{12}\text{C}/^{13}\text{C}$ ratio approaches its equilibrium value very quickly at all metallicities.

Although questions of deep mixing rate (e.g., Smith & Martell 2003) and depth (e.g., Charbonnel et al. 1998) have been studied observationally by many authors, the results available in the literature can be difficult to synthesize into a single conclusion. Many studies focus on one or two particular clusters (e.g., Da Costa & Cottrell 1980, Suntzeff 1981, Trefzger et al. 1983, Lee 1999), or attempt to correlate deep mixing with other cluster properties such as horizontal branch morphology (Cavallo & Nagar 2000), stellar rotational velocity (Chanamé et al. 2005) or cluster ellipticity (Norris 1987). Individual authors and collaborations develop their own analysis tools, and the differences between spectral index definitions, model atmospheres, spectral synthesis engines, and abundance determination methods produce significant systematic differences in different authors’ abundance scales, as is clear from literature-compilation studies such as Smith (2002).

One can construct a phenomenological picture of deep mixing from this heterogeneous information, and it goes roughly as follows: all stars with mass less than $\simeq 2M_{\odot}$ will at some point have their hydrogen-burning shell cross the μ -barrier. The μ -barrier is larger than the critical μ -gradient for deep mixing, so its destruction permits deep mixing to begin. Deep mixing occurs continuously, and involves all material outside the radius where the μ -gradient within the outer H-burning shell is critical. The onset of deep mixing happens lower on the giant branch for higher-metallicity clusters, because their μ -barrier is at smaller radius. However, in higher-metallicity stars the hydrogen-burning shell is more compact (Sweigart & Mengel 1979), so that the radius where the μ -gradient is critical is relatively further out in the hydrogen-burning shell. This means that the material mixed to the surface in higher-metallicity stars is less processed than in low-metallicity stars. Various authors (e.g., Charbonnel et al. 1998, Cassisi et al. 2002) use this relation between metallicity and mixing efficiency to study the structure of the hydrogen-burning shell.

Our goal in this project is to determine the relative efficiency of deep mixing across a broad range of metallicity by measuring present-day carbon abundances and depletion rates from a homogeneous set of globular cluster red giants in similar evolutionary phases. An earlier example of this approach is the study of Bell & Dickens (1980), who found that $[\text{C}/\text{Fe}]$ on the upper RGB of M3, M13 and NGC 6752 correlated with $[\text{Fe}/\text{H}]$ metallicity.

2. THE DATA SET

In order to construct a data set that could be used to compare CH bandstrengths and $[\text{C}/\text{Fe}]$ abundances across a wide range of metallicity, we chose to obtain

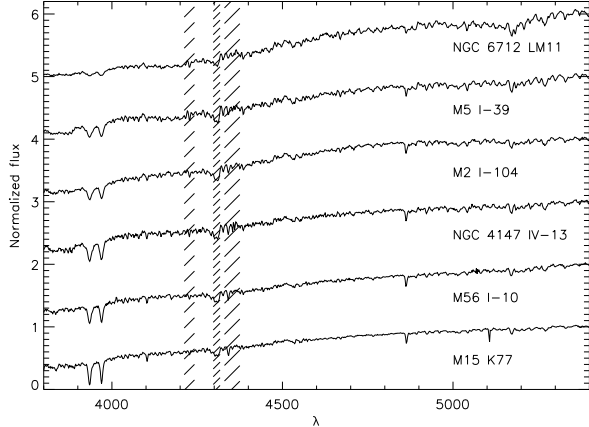


FIG. 1.— Selected spectra from our data set. $M_V \simeq -1.5$ for all stars, $[\text{Fe}/\text{H}]$ varies from -2.25 (M15 K77) to -1.01 (NGC 6712 LM11) in roughly equal steps. The vertical bars with widely spaced shading mark the bandpasses for the comparison bands of $S_2(\text{CH})$, and the narrowly spaced shading marks the corresponding science band.

our data exclusively with the Kast double spectrograph on the Shane 3m telescope at Lick Observatory, devoting 21 nights between July 2004 and August 2006 to the data collection. Using a mirror in place of a dichroic, we directed all light to the blue side of the spectrograph, where the 600/4310 (moderate-resolution) grism produced a pixel spacing of $\simeq 1.8\text{\AA}/\text{pix}$ and a resolution of approximately 5.4\AA over a wavelength range of 3400 to 5400 \AA . The detector at the time was a thinned 1200×400 -pixel Reticon CCD. Table 1 lists names, positions, distance moduli, reddenings, metallicities, and number of stars observed for each globular cluster included in the survey. Metallicities, distance moduli and reddenings were all taken from the February 2003 revision of the online compilation of Harris (1996). Photometry for the individual globular clusters was taken from a combination of original photographic color-magnitude diagram work and proper-motion membership studies: Sandage & Walker (1955) for NGC 4147, Sandage (1953) and Cudworth (1979b) for M3, Arp (1955) and Cudworth (1979c) for M5, Arp (1955) and Cudworth (1979a) for M13, Arp (1955) and Harris et al. (1976) for M10, Cudworth (1976b) for M92, Cudworth (1976a) for M15, Liller (1980) for NGC 6535, Sandage & Smith (1966) and Cudworth (1988) for NGC 6712, Barbon (1965) for M56, and Harris (1975) and Cudworth & Rauscher (1987) for M2.

Targets were observed with a slit width of $1''$, $1.5''$, or $2''$ depending on the seeing. Ideally, three consecutive exposures of each star were taken, with typical exposure times of 1800s, to allow for cosmic ray removal. For 17 of the 42 stars in our sample, there was only time to obtain one or two exposures on a particular night: four of them were observed again at a later date, nine have only two exposures, and four have only one exposure. In all cases, the various exposures were reduced independently, and spectra of each individual star were coadded to produce a final (unfluxed) 1-d spectrum. The standard stars Feige 34, Feige 110, BD +28 4211, and BD +33 2642 were observed with a $9''$ slit aligned with the parallactic angle in an effort to capture maximal UV flux for reliable flux

calibrations. Since Kast sits at Cassegrain focus, spectra of the HeHgCd lamp were taken directly following target spectra, with the same telescope pointing, slit width and dispersive element, to facilitate wavelength calibration and account for flexure.

Data reduction was accomplished with the XIDL LowRedux package made available by J.X. Prochaska at UC Santa Cruz¹. This comprehensive, updated version of the XIDL code used in earlier form in Martell et al. (2008b) handles bias subtraction, flat-fielding, cosmic ray removal, object identification and extraction, sky subtraction, flexure correction, wavelength calibration, atmospheric correction, coadding and flux calibration.

Our targets are bright red giants in the range $-1.0 \geq M_V \geq -2.0$, which generally required 3600-second exposures with Kast to obtain signal-to-noise ratios per pixel just redward of the G band of roughly 150. These stars are all significantly brighter than the RGB luminosity function bump, meaning that any reasonable deep mixing rate will have had time to make a measurable decrement in surface carbon abundance. Figure 1 shows selected spectra from our sample, with metallicities ranging from $[\text{Fe}/\text{H}] = -2.29$ (lowest spectrum) to $[\text{Fe}/\text{H}] = -1.01$ (highest spectrum) in roughly equal steps. As $[\text{Fe}/\text{H}]$ rises, there is a clear increase in the strength of the Mg b and MgH features near 5170 \AA , a slight increase in the strength of the broad CN absorption feature at 4215 \AA , and a reddening of the overall continuum shape that reduces the apparent depth of the Ca II H& K lines at 3935 and 3970 \AA and the CN bandhead at 3883 \AA .

3. ANALYSIS

We use the index $S_2(\text{CH})$, recently defined in Martell et al. (2008a) to be sensitive to carbon abundance and relatively independent of nitrogen abundance over a wide range of metallicity, to quantify the strength of the CH G band in all of our combined, flux-calibrated spectra. As with most spectroscopic indices, $S_2(\text{CH})$ is measured as the magnitude difference between the integrated flux in the relevant absorption feature (the “science band”) and the integrated flux in two nearby relatively absorption-free bands (the “comparison bands”). As discussed in Martell et al. (2008a), the science band for $S_2(\text{CH})$ runs from 4297 \AA to 4317 \AA , and the comparison bands run from 4212 \AA to 4242 \AA and 4330 \AA to 4375 \AA . The bandpasses for $S_2(\text{CH})$ are shown as shaded regions in Figure 1, with the more widely spaced lines marking the comparison bands, and the more closely spaced shading lines marking the science band.

One-sigma errors on measured values of $S_2(\text{CH})$ were determined as in Martell et al. (2008b): for stars observed three or more times, σ_S is calculated as the standard deviation on the mean of the individual index values measured from flux-calibrated, uncombined spectra, and for stars observed twice, $\sigma_S = \frac{0.89 \times \Delta S_2(\text{CH})}{\sqrt{2}}$. Stars observed only once are assumed to have errors in their $S_2(\text{CH})$ values equal to the mean value of σ_S , which is 0.0047.

To convert bandstrengths to $[\text{C}/\text{Fe}]$ abundances, we follow a method similar to that described in Martell et al. (2008b), matching measured values of $S_2(\text{CH})$ to values

¹ available from <http://www.ucolick.org/~xavier/LowRedux/>

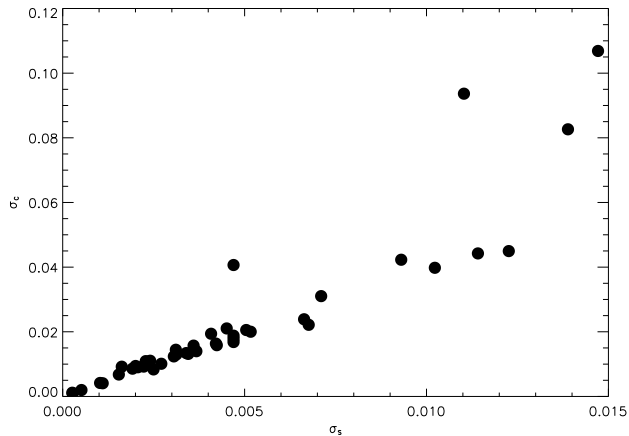


FIG. 2.— Error in calculated $[C/Fe]$ abundance resulting from error in the measured index $S_2(CH)$, for each star in our sample. The abundance error $\sigma_{[C/Fe]}$ is never larger than 0.12 dex, and is almost always smaller than 0.05 dex.

derived from synthetic spectra interpolated to match the data in M_V and $[Fe/H]$ (the “model grid”). We select the subset of the model grid with a canonical $[N/Fe]$ value of +0.6 and interpolate between model $S_2(CH)$ values to find a preliminary $[C/Fe]$. We then interpolate the model grid to that preliminary $[C/Fe]$ value, allow $[N/Fe]$ to have its full range of possible values, and interpolate between model values of the CN bandstrength index $S(3839)$ (Norris et al. 1981) to calculate a preliminary $[N/Fe]$ abundance. If that preliminary $[N/Fe]$ is more than 0.1 dex lower or higher than the canonical value, we interpolate the model grid to match it and repeat the $S_2(CH)$ -matching process to obtain a final $[C/Fe]$ abundance. As a check, we also re-calculate $[N/Fe]$ using the final $[C/Fe]$ value, and we find that the difference between preliminary and final $[C/Fe]$ and $[N/Fe]$ is never large. This is due in large part to the nitrogen-insensitivity of $S_2(CH)$: for a fixed $[C/Fe]$, $[Fe/H]$ and T_{eff} , varying $[N/Fe]$ by large amounts does not change $S_2(CH)$ significantly.

The synthetic spectra employed are quite similar to those used in Martell et al. (2008b): values for T_{eff} and $\log g$ were taken from 12-Gyr Yale-Yonsei (Demarque et al. 2004) isochrones calculated for each cluster metallicity, and MARCS model atmospheres (Gustafsson et al. 1975) and the SSG spectral synthesis program (Bell, Paltoglou, & Trippico 1994 and references therein) were used to generate synthetic spectra. For each individual globular cluster metallicity, $[C/Fe]$ varies from -1.4 to $+0.4$ in steps of 0.2 dex, and $[N/Fe]$ varies from -0.6 to $+2.0$ in steps of 0.2 dex. As in Martell et al. (2008b), other variables such as $^{12}C/^{13}C$, $[O/Fe]$, and v_{turb} were chosen to be consistent with the values used in Briley & Cohen (2001). Synthetic spectra were smoothed to a resolution of 5.4\AA and a pixel spacing of 1.8\AA to match the data.

The errors on our $[C/Fe]$ determinations have several sources, some of which are readily quantifiable: the errors in the measured values of $S_2(CH)$ are generally quite small, and propagate into small noise-based $[C/Fe]$ errors. We determine these noise-based $[C/Fe]$ errors for each star in our sample as half the difference between

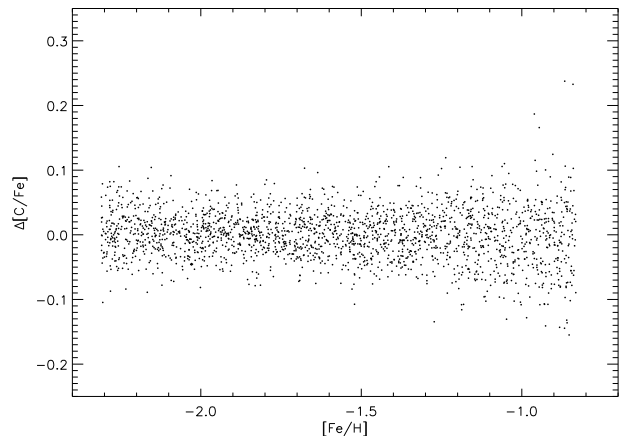


FIG. 3.— Method-based error $\Delta[C/Fe]$ as a function of $[Fe/H]$, for synthetic spectra with $-2.31 \leq [Fe/H] \leq -0.83$, $-1.0 \leq [C/Fe] \leq 0.0$, $0.0 \leq [N/Fe] \leq 1.0$, and 2% Poisson noise. Method-based errors for individual stars in our sample were assigned as the RMS of all points in this figure within ± 0.05 of the $[Fe/H]$ abundance of the parent cluster. Figure adapted from Martell et al. (2008a).

$[C/Fe]$ calculated for $S_2(CH) + \sigma_S$ and $[C/Fe]$ calculated for $S_2(CH) - \sigma_S$. As can be seen in Figure 2, these errors are generally smaller than 0.05 dex, and are all smaller than 0.12 dex. They are also comparable in magnitude to the errors introduced by our index-matching method (the “method-based error”). We calculate a method-based error by choosing a random ($[Fe/H]$, $[C/Fe]$, $[N/Fe]$) point within the abundance range spanned by our model grid, interpolating to find the $S_2(CH)$ value that corresponds, and using that value to re-calculate $[C/Fe]$ assuming a canonical $[N/Fe]$ value of +0.6. The difference between the original input value of $[C/Fe]$ and the calculated value is the method-based error. It is discussed more thoroughly in Martell et al. (2008a), and is a complex function of all of the input abundances. Figure 3, which is adapted from Martell et al. (2008a), shows model-based error for a set of synthetic spectra with 2% Poisson-distributed noise and abundances in the range typically inhabited by globular cluster stars ($-2.31 \leq [Fe/H] \leq -0.83$, $-1.0 \leq [C/Fe] \leq 0.0$, $0.0 \leq [N/Fe] \leq 1.0$), as a function of $[Fe/H]$. The addition of noise to the synthetic spectra was done to make them resemble the observed spectra they are compared to, so that the calculated method-based error would be an accurate representation of the actual error introduced by our carbon-determination method. We assign a method-based error for a given star in our survey as the RMS of all points in Figure 3 that fall within ± 0.05 dex of the $[Fe/H]$ metallicity of its parent cluster.

We combine the noise-based error and the method-based error on calculated $[C/Fe]$ in quadrature, since they are independent, and find that the combined error σ_C never exceeds 0.12 dex, and is usually under 0.05 dex. Table 2 lists cluster name, star name, date observed, cluster $[Fe/H]$, M_V , $S_2(CH)$, σ_S , $[C/Fe]$, and σ_C for each star in our sample. It should be noted that we do not include possible errors in our adopted values of $[Fe/H]$ or the corresponding T_{eff} and $\log(g)$ values taken from the Demarque et al. (2004) isochrones in σ_C .

The matter of systematic offsets to our abundance scale resulting from our flux calibration, temperature scale, or

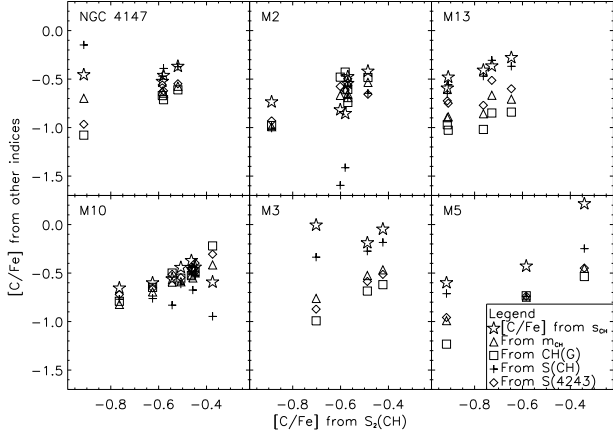


FIG. 4.— Comparison of $[C/Fe]$ values calculated from various CH bandstrength indices, for six of the eleven clusters in our sample. There is generally a vertical offset between abundances derived from the various indices, which may be indicative of errors in flux calibration.

choice of model atmosphere is not as straightforward to assess. We compiled Figure 4 to explore the relationship between $[C/Fe]$ values calculated by using a number of different G-band indices defined in the literature. Each vertical column of points represents one star, with $[C/Fe]$ calculated from the indices s_{CH} (Briley & Smith 1993), m_{CH} (Smith et al. 1996), and $CH(G)$ (Lee 1999) (which were created for studies of red giants in the moderate-metallicity globular clusters M13, M3, and M5) plotted as stars, triangles, and squares, respectively. Crosses and diamonds, respectively, represent $[C/Fe]$ calculated from the indices $S(CH)$ (Martell et al. 2008b) and $S(4243)$ (Briley et al. 1990), which were designed to be used with red giants in the low-metallicity globular clusters M53, M55 and NGC 6397. The comparison and science bandpasses of these indices are given in Table 3. To determine these alternate $[C/Fe]$ values, we followed an index-matching process identical to the one we used to calculate $[C/Fe]$ from $S_2(CH)$.

Interestingly, in Figure 4, there tend to be consistent vertical offsets between $[C/Fe]$ values from the various indices. Since each index covers slightly different wavelength regions, we interpret this to mean that each one captures different information from the spectrum. In general, indices tuned for low-metallicity stars can have wider comparison bands, and do not need to be as carefully defined as indices for high-metallicity clusters, because there are absorption features that are important to avoid in high-metallicity spectra (for example, the CN bandhead at 4215Å). This makes the broader lower-metallicity indices less affected by noise in the observed spectra, but unreliable and often nitrogen-sensitive when used on high-metallicity spectra.

In Figure 4, the values for $[C/Fe]$ calculated from s_{CH} are almost always the highest value for any particular star. Since s_{CH} is defined to have only one comparison band, it is the most susceptible of all the indices we measure to errors in flux calibration or temperature scale. To investigate the possible effects of a mismatch between the overall shape of the data and the synthetic spectra, we performed a test on our M13 spectra, which have a fairly large range in $[C/Fe]$ calculated from the various indices.

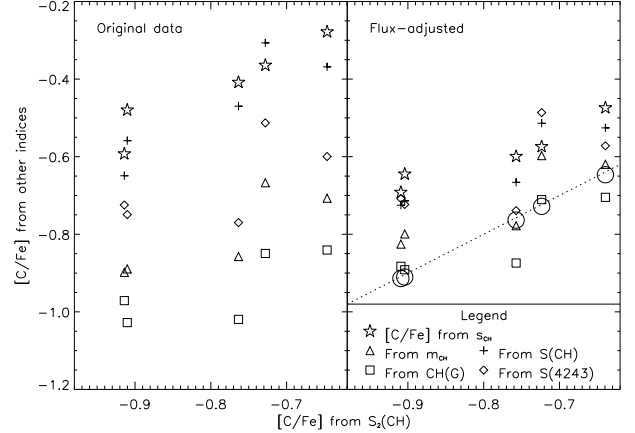


FIG. 5.— Results of the flux-adjustment test: vertical scatter among $[C/Fe]$ values calculated for M13 stars from various S_2 -sensitive indices is greatly reduced when the overall shape of the data continuum is matched to the appropriate synthetic spectrum. The left panel shows $[C/Fe]$ calculated from five G-band indices defined in the literature (y-axis) versus $[C/Fe]$ calculated from $S_2(CH)$ (x-axis) for the five M13 stars in our data set. The right panel shows the results of the same measurements made on data adjusted to match the overall shape of abundance-matched synthetic spectra. Large circles in the right panel show the $[C/Fe]$ values calculated from $S_2(CH)$ and the non-adjusted data spectra, and lie very close to the dashed line showing 1:1 correspondence.

For each of the five M13 stars in our sample, we adjusted the flux calibration to match the overall spectral shape of an appropriate synthetic spectrum. We fit a parabola to fairly absorption-free regions between 4000Å and 4500Å in both the data and interpolated-synthetic spectra, and used the ratio of those two curves to adjust the overall shape of the data to match the synthetic spectra. The left panel of Figure 5 is the same as the M13 panel of Figure 4, and shows the $[C/Fe]$ abundances calculated from the various CH indices. The right panel shows $[C/Fe]$ abundances calculated from the same CH indices, measured from the flux-adjusted spectra, and the vertical scatter is considerably decreased. The large circles in the right panel show the $S_2(CH)$ -derived $[C/Fe]$ values, measured from the original (non-flux-adjusted) spectra, and they fall almost exactly on the dashed line showing 1:1 correspondence. We make two conclusions from this exercise: first, that disagreement between $[C/Fe]$ calculated from indices that purport to measure the same underlying abundance can be a sign of flux-calibration or temperature-scale errors, and second, that continuum-division is likely preferable to flux-calibration, so that this potential source of error can be avoided altogether.

However, the $[C/Fe]$ values calculated from $S_2(CH)$ are barely changed by the flux adjustment. As discussed in Martell et al. (2008a), $S_2(CH)$ was designed specifically to be fairly sensitive to carbon abundance and insensitive to nitrogen abundance over a wide range in metallicity. Therefore we feel that our $[C/Fe]$ values are fairly robust, and we choose to use $S_2(CH)$ for carbon determinations in all of our data, rather than building a patchwork of metallicity-tuned indices and correcting for estimated systemic offsets. In addition, since our goal is a differential measurement of $[C/Fe]$ between stars of varying $[Fe/H]$, the absolute zeropoint of our $[C/Fe]$ abundance scale is not vital to our result.

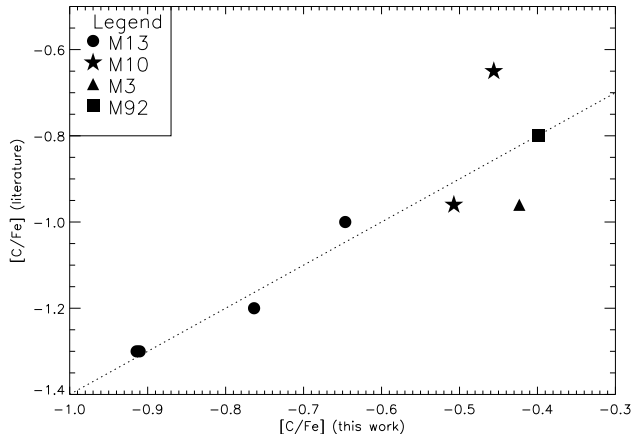


FIG. 6.— Comparison of our $[C/Fe]$ values calculated from $S_2(CH)$ with literature carbon abundances. Literature data for M3 and M13 are from Suntzeff (1981), the M10 data are from Smith et al. (2005), and the M92 data point is taken from Bellman et al. (2001). The dashed line shows the line $[C/Fe]_{\text{thiswork}} = [C/Fe]_{\text{lit}} + 0.4$, which is consistent with the literature-compilation studies of Smith & Briley (2006) and Smith (2002).

In Figure 6 we plot $[C/Fe]$ derived from our $S_2(CH)$ measurements versus $[C/Fe]$ values taken from the literature, for the eight stars in our sample with published carbon abundances. Carbon abundances in M3 and M13 were taken from Suntzeff (1981), carbon abundance values for M10 are taken from Smith et al. (2005), and the single point for M92 is from Bellman et al. (2001). The data compilations of Smith & Briley (2006) and Smith (2002) find that Suntzeff (1981) carbon abundances tend to fall $\simeq 0.35$ dex below other reported carbon abundances in M13 and M3. It is therefore encouraging to find that the dashed line in Figure 6, which shows the relation $[C/Fe]_{\text{lit}} = [C/Fe]_{\text{thiswork}} - 0.4$, traces the data so closely. As for the M10 and M92 stars, our $[C/Fe]$ values are clearly larger than those reported in the literature, but with such small crossover samples it is difficult to describe this decisively as a systematic offset.

4. RESULTS

A functional form for the evolution of carbon abundance with time may be found by considering the stellar envelope as a simple system with a constant mass M and mixing rate \dot{M} . If deep mixing removes carbon from the combined convective envelope plus atmosphere at a rate $-\dot{M} \times X_{C,env}$ (where $X_{C,env}$ is the mass fraction of carbon in the envelope at time t), and introduces it at a rate $\dot{M} \times X_{C,hbs}$ (where $X_{C,hbs}$ is the mass fraction of carbon in the hydrogen-burning shell), then the rate of change of atmospheric carbon abundance can be written as

$$\frac{d(MX_{C,env})}{dt} = \dot{M}(X_{C,hbs} - X_{C,env})$$

The equilibrium abundance of carbon in the CNO cycle is quite small, so this integrates simply to

$$X_{C,env} \propto \exp^{-(\dot{M}/M)t}$$

where M/\dot{M} can be thought of as the characteristic timescale for mixing. Since $[C/Fe]$ is a logarithmic measure of carbon abundance, an exponential decline

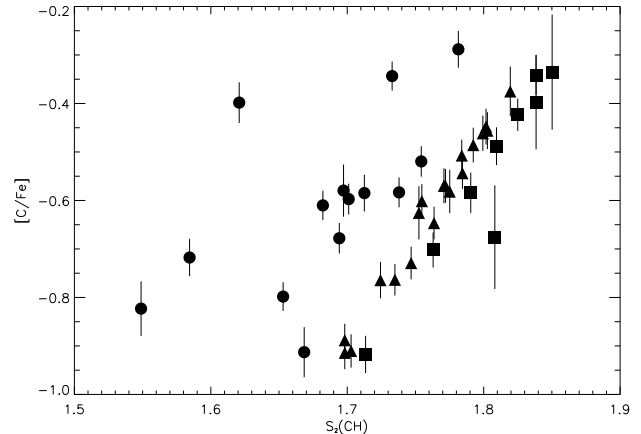


FIG. 7.— Derived $[C/Fe]$ abundance versus measured $S_2(CH)$ bandstrength for all stars in our survey, with total error bars as described in the text and symbols denoting three broad $[Fe/H]$ bins. Circles represent stars with $[Fe/H] \leq -1.7$, triangles are for the bin $-1.7 \leq [Fe/H] < -1.4$, and squares show stars with $[Fe/H] \geq -1.4$. Equal $[C/Fe]$ abundances are expressed as different CH bandstrengths depending on $[Fe/H]$.

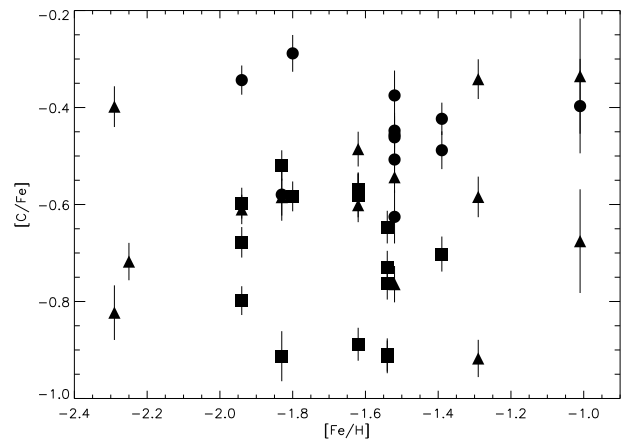


FIG. 8.— Derived $[C/Fe]$ abundance with error bars, as in Figure 7, versus $[Fe/H]$. Here symbols denote three broad M_V bins. Circles show stars with $M_V \geq -1.3$, triangles are for the bin $-1.3 > M_V \geq -1.6$, and squares are for stars with $M_V < -1.6$. Although the faintest and brightest bins separate fairly well into high and low carbon abundances, respectively, it is unclear from this plot whether low-metallicity stars experience more rapid carbon depletion than high-metallicity stars.

in $X_{C,env}$ will result in a linear decline in $[C/Fe]$ with time. Smith & Martell (2003) find a linear decline in $[C/Fe]$ with M_V among bright red giants in the field and in the globular clusters M92, NGC 6397, and M3, with a slope of 0.22 dex/magnitude. The field-star study of Gratton et al. (2000) finds a linear trend in $[C/Fe]$ with $\log(L/L_\odot)$. According to Demarque et al. (2004) evolutionary tracks, the $\log(L/L_\odot)$ - t relationship is not exactly linear for post-bump RGB stars ($1.8 \leq \log(L/L_\odot) \leq 2.6$), but it is sufficiently close that a linear $[C/Fe] - M_V$ or $[C/Fe] - \log(L/L_\odot)$ relation suggests a fairly linear $[C/Fe] - t$ relation as well.

Figure 7 shows calculated $[C/Fe]$ versus measured $S_2(CH)$ for our sample, with symbols indicating three broad metallicity bins. Circles are stars from clusters with $[Fe/H] \leq -1.7$, triangles represent stars with

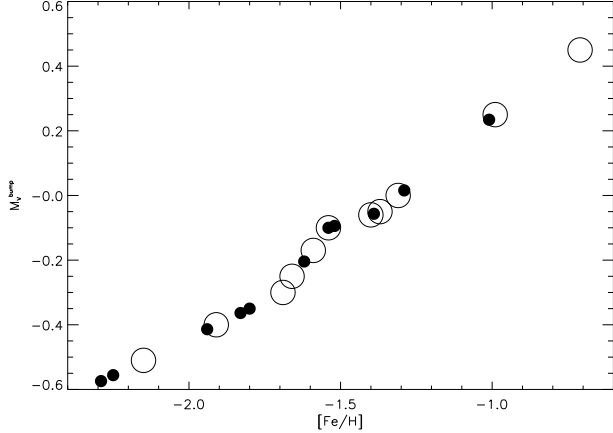


FIG. 9.— The relation between the absolute M_V magnitude of the “bump” in the red giant branch luminosity function and metallicity. Large circles are data from 11 globular clusters observed in Fusi Pecci et al. (1990), and small circles are the values for the globular clusters in our sample, interpolated linearly from the Fusi Pecci et al. (1990) data.

$-1.7 \leq [\text{Fe}/\text{H}] \leq -1.4$, and squares are for stars with $[\text{Fe}/\text{H}] \geq -1.4$. It can be clearly seen that equal carbon abundances are expressed as lower CH bandstrengths at lower metallicity. The error bars shown are equal to $\pm\sigma_C$. Figure 8 shows calculated $[\text{C}/\text{Fe}]$ with error bars as a function of $[\text{Fe}/\text{H}]$, and here the symbols represent three broad luminosity bins. These bins have the same sense as in Figure 7, with the faintest stars represented by circles and the brightest stars plotted as squares. Although the faintest and brightest stars occupy mostly separate regions in this figure, there is not a clear trend between $[\text{C}/\text{Fe}]$ and $[\text{Fe}/\text{H}]$. However, the lack of a clear correlation in Figure 8 does not necessarily mean that there is no dependence of deep mixing rate on stellar metallicity.

The question of how much time each observed star has spent in the deep mixing phase is the key to interpreting our data: we selected targets with similar absolute magnitudes, but it is well-known observationally (Fusi Pecci et al. 1990) and theoretically (Cassisi & Salaris 1997) that the RGB bump occurs at lower luminosity in more metal-rich globular clusters. In addition, low-metallicity red giants evolve more quickly than high-metallicity red giants of the same mass (e.g., Riello et al. 2003). As a result, the $M_V = -1.5$ red giants in the metal-rich end of our sample have been mixing for far longer than their metal-poor counterparts. In order to study deep mixing efficiency with our data set, we must convert our $[\text{C}/\text{Fe}]$ values, which are a function of both $[\text{Fe}/\text{H}]$ and time, to some time-invariant quantity. We choose to do this by converting present-day $[\text{C}/\text{Fe}]$ abundances to a carbon depletion rate per Gyr. This is a two-step process: we must first calculate the absolute magnitude of the RGB bump, M_V^{bump} , for each individual cluster, and then for each star we must convert the V magnitude height above the bump, ΔM_V^{bump} , into a time since the onset of deep mixing.

We use the observational study of Fusi Pecci et al. (1990) to calculate M_V^{bump} for each cluster in our survey. As can be seen in Figure 9, there is a nearly-linear relationship between observed M_V^{bump} (plotted as

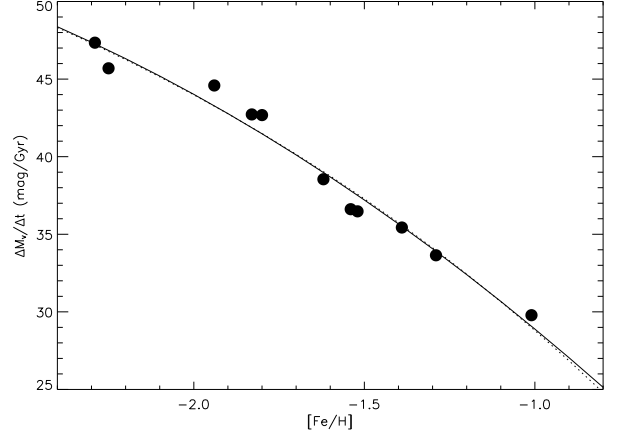


FIG. 10.— Rate of evolution $\Delta M_V/\Delta t$ versus $[\text{Fe}/\text{H}]$ for the eleven globular clusters in our sample, calculated using Yale-Yonsei (Demarque et al. 2004) isochrones and evolutionary tracks in the range $M_V^{\text{bump}} \geq M_V \geq -1.5$. The solid curve is the best-fit polynomial, and the dashed curve is the best-fit exponential.

large open circles) and $[\text{Fe}/\text{H}]$. We calculate M_V^{bump} for the eleven clusters in our sample by a simple linear interpolation from the Fusi Pecci et al. (1990) data. The conversion from ΔM_V^{bump} to Δt^{bump} is based on Yale-Yonsei (Demarque et al. 2004) isochrones and evolutionary tracks. For each cluster metallicity, we created an evolutionary track for a star with appropriate metallicity and a mass taken from the $M_V = -1.5$ point in a metallicity-matched 12 Gyr YY isochrone. We then chose points in the evolutionary track near M_V^{bump} and $M_V = -1.5$, and we calculate $\Delta M_V/\Delta t$ based on those points. Figure 10 shows our calculated values for $\Delta M_V/\Delta t$ for all clusters in our sample, along with a best-fit polynomial (solid curve) and a best-fit exponential (dashed curve), which are nearly identical.

Combining these two steps, we calculate the carbon depletion rate $\Delta[\text{C}/\text{Fe}]/\Delta t$ as $[\text{C}/\text{Fe}]/\Delta M_V^{\text{bump}} \times \Delta M_V/\Delta t$, assuming that the initial $[\text{C}/\text{Fe}]$ abundance is solar, and that deep mixing begins at the RGB bump for all stars. Figure 11 shows $\Delta[\text{C}/\text{Fe}]/\Delta t$ versus $[\text{Fe}/\text{H}]$ for all stars in our sample, and there is a clear downward trend in carbon depletion rate as metallicity increases. We see no break or corner in the relation between $\Delta[\text{C}/\text{Fe}]/\Delta t$ and $[\text{Fe}/\text{H}]$, indicating that mixing is never completely prohibited in our sample. This may happen at metallicities above $[\text{Fe}/\text{H}] = -1.0$, if the hydrogen-burning shell is so compressed that the critical μ -gradient is reached outside it. Our result is in agreement with the theoretical predictions of Charbonnel & Zahn (2007), and confirms that the process of deep mixing is less effective in relatively high-metallicity red giants.

5. CONCLUSIONS AND FUTURE WORK

In summary, the results of this work show that within the $[\text{Fe}/\text{H}]$ range -2.2 to -1.0 dex the rate of deep mixing varies with metallicity. We measure CH bandstrength using the index $S_2(\text{CH})$, which was designed to be valid across a broad range in $[\text{Fe}/\text{H}]$ (Martell et al. 2008a). Carbon abundances are determined by matching CH bandstrengths measured from the data to bandstrengths measured from specifically-designed grids of SSG syn-

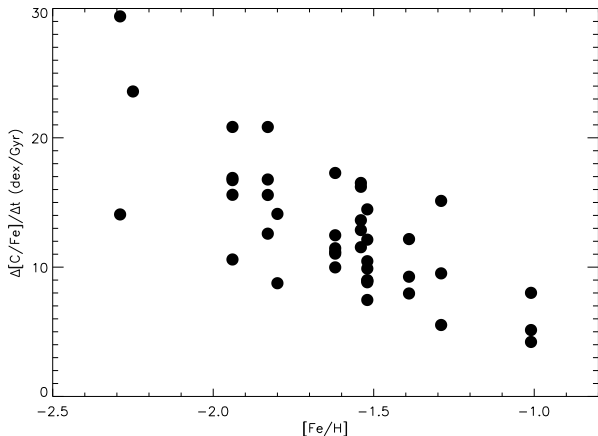


FIG. 11.— Carbon depletion rate $\Delta[\text{C}/\text{Fe}]/\Delta t$ versus $[\text{Fe}/\text{H}]$ for all of the stars in our sample. There is a clear downward trend with rising metallicity, a result predicted by the deep mixing models of, e.g., Charbonnel & Zahn (2007).

thetic spectra. Under the assumption (Charbonnel et al. 1998) that deep mixing begins at the RGB luminosity function bump, we establish the carbon depletion rate for a given star as the change in its $[\text{C}/\text{Fe}]$ from an initial solar value divided by the time elapsed since the onset of mixing. Since the RGB luminosity function bump is fainter in high-metallicity globular clusters than in lower-metallicity globular clusters, and higher-metallicity red giants evolve more slowly than lower metallicity red giants, higher-metallicity stars at a given absolute magnitude qualitatively ought to have spent more time mixing than their lower-metallicity counterparts. In order to quantify the time spent mixing as a function of metallicity and absolute V magnitude, we interpolate the Fusi Pecci et al. (1990) observational data on M_V^{bump} as a function of metallicity to the metallicities of the clusters in our study, then use metallicity-appropriate Yale-Yonsei (Demarque et al. 2004) isochrones to convert ΔM_V^{bump} for each individual star into Δt^{bump} . As can be seen in Figure 10, the lower-metallicity red giants do evolve more quickly, and therefore spend less time mixing than the higher-metallicity red giants in this study. However, dividing $[\text{C}/\text{Fe}]$ by Δt^{bump} for each individual star produces the result that the deep mixing rate is roughly twice as large at $[\text{Fe}/\text{H}] = -2.0$ than at $[\text{Fe}/\text{H}] = -1.0$, as can be seen in Figure 11.

This present analysis includes some assumptions worth noting, since they may need to be more carefully examined if this result is to provide constraints for theoretical models of deep mixing. To express $X_{C,env}$ as a straightforward exponential in time, we hold the mass of the stellar envelope constant, though it shrinks continuously as the hydrogen-burning shell proceeds outward (Denissenkov & Vandenberg 2003). We also hold the mixing rate \dot{M} constant, though it is controlled by the structure of the hydrogen-burning shell, and may well evolve. In addition, we implicitly assume in constructing Figure 11 that all stars have equal (and solar) initial abundances of carbon. A primordial depletion of ~ 0.3 dex in a subset of our sample would thus be misinterpreted as an artificially high mixing rate in those stars. A study of carbon abundances in fainter post-

bump red giants, or pre-bump giants, in the globular clusters included in this study, would allow for direct calculation of $\Delta[\text{C}/\text{Fe}]/\Delta t$ without assumptions about the initial carbon abundance. In addition, a study of carbon depletion rates in high-metallicity red giants, either in old open clusters or in high-metallicity globular clusters, would allow an estimation of the maximum metallicity at which deep mixing still operates. That maximum metallicity would be helpful for constraining the various models of deep mixing. Nevertheless, our fundamental result, that carbon depletion proceeds more quickly in low-metallicity globular cluster red giants than in their high-metallicity counterparts, is robust, and provides a clear affirmation of present theoretical models.

TABLE 1

Cluster ID	RA (J2000)	δ (J2000)	$(m - M)_V$	$E(B - V)$	[Fe/H]	N_{obs}
NGC 4147	12 10 06.2	+18 32 31	16.48	0.02	-1.83	4
NGC 5727 (M3)	13 42 11.2	-28 22 32	15.08	0.01	-1.39	3
NGC 5904 (M5)	15 18 33.8	+02 04 58	14.46	0.03	-1.29	3
NGC 6205 (M13)	16 41 41.5	+36 27 37	14.45	0.02	-1.54	5
NGC 6254 (M10)	16 57 08.9	-04 05 58	14.08	0.28	-1.52	8
NGC 6341 (M92)	17 17 07.3	+43 08 11	14.64	0.02	-2.29	2
NGC 6535	18 03 50.7	-00 17 49	15.22	0.34	-1.80	2
NGC 6712	18 53 04.3	-08 42 22	15.60	0.45	-1.01	3
NGC 6779 (M56)	19 16 35.5	+30 11 05	15.65	0.20	-1.94	5
NGC 7078 (M15)	21 29 58.3	+12 10 01	15.23	0.10	-2.25	1
NGC 7089 (M2)	21 33 29.3	-00 49 23	15.49	0.06	-1.62	6

TABLE 2

Cluster ID	Star ID	Date obs.	M_V	[Fe/H]	$S_2(CH)$	σ_S	[C/Fe]	σ_C
M10	II-105	2006-06-03	-1.23	-1.52	1.753	0.0114	-0.625	0.0549
M10	III-73	2006-06-03	-1.22	-1.52	1.784	0.0011	-0.507	0.0327
M10	III-85	2006-06-03	-1.38	-1.52	1.784	0.5153	-0.544	0.0325
M10	IV-30	2006-06-03	-1.28	-1.52	1.803	0.0052	-0.456	0.0381
M10	I-15	2004-07-12	-1.22	-1.52	1.799	0.0047	-0.461	0.0365
M10	III-93	2004-07-12	-1.18	-1.52	1.802	0.0047	-0.448	0.0370
M10	III-97	2004-07-12	-1.41	-1.52	1.724	0.0047	-0.764	0.0375
M10	I-12	2005-07-12	-1.14	-1.52	1.819	0.0102	0.375	0.0513
M13	IV-53	2005-04-17	-1.77	-1.54	1.747	0.0019	-0.729	0.0336
M13	II-33	2006-06-01	-1.78	-1.54	1.764	0.0021	-0.647	0.0337
M13	III-52	2006-06-01	-1.78	-1.54	1.735	0.2635	-0.763	0.0325
M13	II-57	2006-06-02	-1.75	-1.54	1.703	0.0023	-0.910	0.0342
M13	III-18	2006-06-02	-1.68	-1.54	1.698	0.0020	-0.914	0.0338
M15	K77	2005-09-06	-1.53	-2.25	1.584	0.0016	-0.718	0.0386
M2	I-103	2005-07-13	-1.92	-1.62	1.775	0.0071	-0.582	0.0447
M2	I-104	2005-07-13	-1.52	-1.62	1.792	0.0042	-0.486	0.0359
M2	I-298	2005-09-07	-1.46	-1.62	1.755	0.0037	-0.601	0.0351
M2	I-190	2005-09-08	-1.75	-1.62	1.698	0.0024	-0.888	0.0340
M2	II-60	2005-09-09	-1.69	-1.62	1.772	0.0034	-0.570	0.0348
M2	II-71	2005-09-09	-1.64	-1.62	1.771	0.0042	-0.570	0.0361
M3	BC	2006-05-31	-1.24	-1.39	1.825	0.0010	-0.423	0.0333
M3	I-46	2006-05-31	-1.26	-1.39	1.809	0.0050	-0.488	0.0389
M3	V-80	2006-06-02	-1.61	-1.39	1.763	0.0031	-0.702	0.0361
M5	I-39	2006-06-01	-1.39	-1.29	1.838	0.0041	-0.342	0.0410
M5	IV-34	2006-06-02	-1.41	-1.29	1.791	0.0045	-0.584	0.0418
M5	IV-49	2006-06-03	-1.32	-1.29	1.713	0.0031	-0.917	0.0384
M56	I-10	2006-08-30	-1.53	-1.94	1.682	0.0022	-0.610	0.0304
M56	E-48	2006-08-31	-1.95	-1.94	1.694	0.0031	-0.678	0.0315
M56	I-141	2005-09-06	-1.22	-1.94	1.733	0.0025	-0.343	0.0301
M56	E-22	2005-09-07	-1.78	-1.94	1.701	0.0035	-0.597	0.0318
M56	I-66	2005-09-07	-1.78	-1.94	1.653	0.0015	-0.798	0.0297
M92	II-70	2006-05-31	-1.40	-2.29	1.621	0.0036	-0.398	0.0420
M92	IV-94	2006-05-31	-1.44	-2.29	1.549	0.0047	-0.823	0.0563
NGC 4147	II-14	2005-02-01	-1.150	-1.83	1.697	0.0123	-0.580	0.0539
NGC 4147	II-30	2005-02-01	-1.760	-1.83	1.754	0.0027	-0.519	0.0313
NGC 4147	II-45	2005-02-02	-1.960	-1.83	1.668	0.0093	-0.913	0.0516
NGC 4147	IV-13	2005-02-02	-1.390	-1.83	1.713	0.0066	-0.585	0.0381
NGC 6535	13	2004-07-13	-1.71	-1.80	1.738	0.2743	-0.583	0.0308
NGC 6535	19	2004-07-13	-0.990	-1.80	1.781	0.0068	-0.288	0.0379
NGC 6712	KC564	2005-07-13	-1.430	-1.01	1.850	0.0147	-0.335	0.1187
NGC 6712	LM11	2005-07-13	-1.200	-1.01	1.838	0.0139	-0.397	0.0974
NGC 6712	B66	2006-08-31	-1.57	-1.01	1.808	0.0110	-0.676	0.1069

TABLE 3

Index	Blue comparison band (Å)	Science band (Å)	Red comparison band (Å)	Reference
<i>sCH</i>	4220-4280	4280-4320	-	Briley & Smith (1993)
<i>mCH</i>	4080-4130	4270-4320	4420-4470	Smith et al. (1996)
<i>CH(G)</i>	4230-4260	4270-4320	4390-4420	Lee (1999)
<i>S(CH)</i>	4050-4100	4280-4320	4330-4350	Martell et al. (2008b)
<i>S(4243)</i>	-	4290-4318	4314-4322	Briley et al. (1990)
<i>S₂(CH)</i>	4212-4242	4297-4317	4330-4375	Martell et al. (2008a)

REFERENCES

- Arp, H. C. 1955, *AJ*, 60, 317
- Barbon, R. 1965, *Contributions dell'Osservatorio Astrofisica dell'Universita di Padova in Asiago*, 175, 63
- Bell, R. A. & Dickens, R. J. 1980, *ApJ*, 242, 657
- Bell, R. A., Paltoglou, G., & Tripicco, M. J. 1994, *MNRAS*, 268, 771
- Bellman, S., Briley, M. M., Smith, G. H., & Claver, C. F. 2001, *PASP*, 113, 326
- Briley, M. M., Bell, R. A., Hoban, S., & Dickens, R. J. 1990, *ApJ*, 359, 307
- Briley, M. M. & Cohen, J. G. 2001, *AJ*, 122, 242
- Briley, M. M. & Smith, G. H. 1993, *PASP*, 105, 1260
- Carbon, D. F., Romanishin, W., Langer, G. E., Butler, D., Kemper, E., Trefzger, C. F., Kraft, R. P., & Suntzeff, N. B. 1982, *ApJS*, 49, 207
- Cassisi, S. & Salaris, M. 1997, *MNRAS*, 285, 593
- Cassisi, S., Salaris, M., & Bono, G. 2002, *ApJ*, 565, 1231
- Cavallo, R. M. & Nagar, N. M. 2000, *AJ*, 120, 1364
- Chanamé, J., Pinsonneault, M., & Terndrup, D. M. 2005, *ApJ*, 631, 540
- Charbonnel, C. 1994, *A&A*, 282, 811
- , 1995, *ApJ*, 453, L41
- Charbonnel, C., Brown, J. A., & Wallerstein, G. 1998, *A&A*, 332, 204
- Charbonnel, C. & Zahn, J.-P. 2007, *A&A*, 467, L15
- Cudworth, K. 1979a, *AJ*, 84, 1005
- Cudworth, K. M. 1976a, *AJ*, 81, 519
- , 1976b, *AJ*, 81, 975
- , 1979b, *AJ*, 84, 1312
- , 1979c, *AJ*, 84, 1866
- , 1988, *AJ*, 96, 105
- Cudworth, K. M. & Rauscher, B. J. 1987, *AJ*, 93, 856
- Da Costa, G. S. & Cottrell, P. L. 1980, *ApJ*, 236, L83
- Demarque, P., Woo, J.-H., Kim, Y.-C., & Yi, S. K. 2004, *ApJS*, 155, 667
- Denissenkov, P. A. & Tout, C. A. 2000, *MNRAS*, 316, 395
- Denissenkov, P. A. & Vandenberg, D. A. 2003, *ApJ*, 593, 509
- Eggleton, P. P., Dearborn, D. S. P., & Lattanzio, J. C. 2008, *ApJ*, 677, 581
- Fusi Pecci, F., Ferraro, F. R., Crocker, D. A., Rood, R. T., & Buonanno, R. 1990, *A&A*, 238, 95
- Gilroy, K. K. 1989, *ApJ*, 347, 835
- Gratton, R. G., Sneden, C., Carretta, E., & Bragaglia, A. 2000, *A&A*, 354, 169
- Gustafsson, B., Bell, R. A., Eriksson, K., & Nordlund, A. 1975, *A&A*, 42, 407
- Harris, W. E. 1975, *ApJS*, 29, 397
- , 1996, *AJ*, 112, 1487
- Harris, W. E., Racine, R., & de Roux, J. 1976, *ApJS*, 31, 13
- Iben, I. J. 1965, *ApJ*, 142, 1447
- , 1968, *ApJ*, 154, 581
- Langer, G. E., Kraft, R. P., Carbon, D. F., Friel, E., & Oke, J. B. 1986, *PASP*, 98, 473
- Lee, S.-G. 1999, *AJ*, 118, 920
- Liller, M. H. 1980, *AJ*, 85, 1480
- Martell, S. L., Smith, G. H., & Briley, M. M. 2008a, *PASP*, 120, 839
- , 2008b, *PASP*, 120, 7
- Norris, J. 1987, *ApJ*, 313, L65
- Norris, J., Cottrell, P. L., Freeman, K. C., & Da Costa, G. S. 1981, *ApJ*, 244, 205
- Palacios, A., Charbonnel, C., Talon, S., & Siess, L. 2006, *A&A*, 453, 261
- Riello, M., Cassisi, S., Piotto, G., Recio-Blanco, A., De Angeli, F., Salaris, M., Pietrinferni, A., Bono, G., & Zoccali, M. 2003, *A&A*, 410, 553
- Sandage, A. & Smith, L. L. 1966, *ApJ*, 144, 886
- Sandage, A. R. 1953, *AJ*, 58, 61
- Sandage, A. R. & Walker, M. F. 1955, *AJ*, 60, 230
- Smith, G. H. 2002, *PASP*, 114, 1097
- Smith, G. H. & Briley, M. M. 2006, *PASP*, 118, 740
- Smith, G. H., Briley, M. M., & Harbeck, D. 2005, *AJ*, 129, 1589
- Smith, G. H. & Martell, S. L. 2003, *PASP*, 115, 1211
- Smith, G. H., Shetrone, M. D., Bell, R. A., Churchill, C. W., & Briley, M. M. 1996, *AJ*, 112, 1511
- Suntzeff, N. B. 1981, *ApJS*, 47, 1
- Suntzeff, N. B. & Smith, V. V. 1991, *ApJ*, 381, 160
- Sweigart, A. V. & Mengel, J. G. 1979, *ApJ*, 229, 624
- Trefzger, C. F., Langer, G. E., Carbon, D. F., Suntzeff, N. B., & Kraft, R. P. 1983, *ApJ*, 266, 144
- Ulrich, R. K. 1972, *ApJ*, 172, 165
- Weiss, A. & Charbonnel, C. 2004, *Memorie della Societa Astronomica Italiana*, 75, 347
- Zoccali, M., Cassisi, S., Piotto, G., Bono, G., & Salaris, M. 1999, *ApJ*, 518, L49